Research Square

Preprints are preliminary reports that have not undergone peer review.
They should not be considered conclusive, used to inform clinical practice,
or referenced by the media as validated information.

Acid leaching reorganizes hierarchical nanoporous alteration layers on borosilicate glass

Tadanobu Hiratsuka
Tokyo City University
Sota Maeda
Tokyo City University
Iori Funayama
Tokyo City University
Rinka Kato
Tokyo City University
Takuya Fujima
tfujima@tcu.ac.jp

Tokyo City University

Article

Keywords:

Posted Date: November 6th, 2026

DOI: https://doi.org/10.21203/rs.3.rs-11370359/v1

License: This work is licensed under a Creative Commons Attribution 4.0 International License.
Read Full License

Additional Declarations: No competing interests reported.

Abstract

Aqueous corrosion of silicate glass produces surface alteration layers whose formation may involve both leaching/in situ reorganization and interface-coupled dissolution–precipitation (ICDP). Here, selective acid leaching combined with focused ion beam scanning electron microscopy tomography, transmission electron microscopy–energy-dispersive X-ray spectroscopy, and X-ray photoelectron spectroscopy was used to probe aluminum in a hierarchical nanoporous layer formed on borosilicate glass. Acid leaching removed aluminum almost completely while retaining a continuous porous silicate layer, consistent with an acid-soluble hydroxylated Al-containing secondary phase located outside, rather than incorporated into, the silicate network. Its removal thinned the segmented solid phase and altered the depth-dependent porosity. Associated shifts in optical reflectance and water-droplet spreading were consistent with changes in layer thickness and pore structure. These findings support contributions from both ICDP-type and leaching/in situ reorganization processes and identify aluminum speciation as an important factor governing alteration-layer structure and response.

Introduction

Silicate glasses are used across an exceptionally broad range of applications. Borosilicate glass in particular is widely employed as a matrix for the stable immobilization of fission products and minor actinides generated by the reprocessing of spent nuclear fuel.[1] Because glass is exposed to aqueous environments in many of these applications, understanding glass–water interactions is essential for ensuring the long-term performance and reliability of the material.[2]

When exposed to water, silicate glass forms a surface alteration layer (SAL), yet the mechanism by which this layer forms remains unresolved.[2,3] Two contrasting models have been proposed. In the first, a leaching / in-situ reorganization model, the porous alteration layer develops through ion exchange between alkali ions in the glass and protons in solution, hydrolysis of the silicate network, and subsequent structural reorganization.[4–6] In the second, the interface-coupled dissolution–precipitation (ICDP) model, the glass constituents dissolve congruently and specific elements become locally supersaturated near the glass–water interface, so that the alteration layer precipitates and grows as a secondary phase.[7–10] Both models are supported experimentally, and which mechanism dominates is thought to depend on conditions such as pH, temperature, and solution chemistry.[2] No single model can account for all glass-corrosion phenomena with a single mechanism.[2,11]

Among the SALs produced by such corrosion processes, some represent a unique case in which the structure can be precisely controlled by the corrosion conditions and in which the resulting structural change is directly reflected in the functional properties. A prominent example is the hierarchical nanoporous layer (HNL) glass.[12] The HNL forms on silicate glass substrates—such as soda-lime and borosilicate glasses—through a one-pot process in which the substrate is etched in a heated basic aqueous solution (typically an $NaHCO_3$ solution). The resulting HNL possesses a three-dimensional,

sponge-like porous structure in which the pore diameter varies continuously from the glass surface toward the bulk (a hierarchical structure with pore diameters of several tens of nanometres near the surface, decreasing to a few nanometres near the bulk interface). The HNL thickness can be readily controlled from several tens of nanometres to well over several tens of micrometres by adjusting the etching conditions (temperature, time, and solution composition). Because the HNL thickness determines the depth profile of the effective refractive index, changing the corrosion conditions modulates the antireflective properties across the visible range. The three-dimensional continuous porous structure and large internal surface area promote capillary infiltration, giving rise to a long-lived superhydrophilicity with a water contact angle of about 5°, which in turn provides antifogging and antifouling functionality.[12,13] Coating with polydimethylsiloxane (PDMS) imparts superhydrophobicity and droplet-shedding behavior while preserving the intrinsic low-reflectivity of the HNL.[14] The precipitation and immobilization of perovskite nanocrystals within the pores yields a mechanically robust nanoparticle-dispersion layer,[15] and impregnation with (PSS-free) PEDOT allows the HNL to function as a transparent conductive film that simultaneously achieves a visible transmittance above 85% and a sheet resistance of several hundred Ω sq^{-1} without rare-earth metals or ITO.[16] These findings suggest the possibility of reconceiving glass corrosion not as unavoidable degradation but as a process through which structure and function can be designed.

Nevertheless, the chemical and physical mechanisms by which a hierarchical gradient structure such as the HNL forms remain insufficiently understood. Clarifying the formation mechanism is an important challenge that would not only provide design guidelines for the HNL but also contribute to a broader understanding of corrosion reactions at glass–water interfaces. In the aqueous corrosion of silicate glass, it is widely known that Na in the glass undergoes ion exchange with protons in solution and is preferentially leached from the near-surface region.[2,17–19] In the HNL, a depth-dependent Na concentration gradient from the surface to the interior has likewise been confirmed by elemental depth analysis, showing that ion-exchange leaching of Na proceeds during HNL formation.[20] In previous work, aluminum was reported to become markedly concentrated within the HNL structure during its formation.[20] It is therefore considered that both a leaching / in-situ reorganization process, based on the ion-exchange leaching of Na, and an ICDP-type process related to the behavior of aluminum are jointly involved in HNL formation.

However, it remains unclear whether the aluminum concentrated within the HNL is a structural component covalently incorporated into the network skeleton or a secondary phase deposited outside the skeleton (on the pore-wall side). This distinction is a core question in elucidating the HNL formation mechanism: if aluminum resides within the skeleton, structural stabilization through network modification is implied, whereas if it exists as a secondary phase outside the skeleton, an ICDP-type re-precipitation and immobilization process is dominant. When aluminum is covalently incorporated into the silicate skeleton as a network-forming, tetrahedral AlO_4 species, the network connectivity and the chemical durability are reported to increase.[23] Distinguishing whether the aluminum contributes to the

durability of the HNL skeleton or is merely an accompanying secondary phase outside the skeleton is therefore directly relevant to understanding the chemical stability of the HNL.

In the present study, we exploited a selective-leaching experiment based on acid treatment: if aluminum is present as an acid-soluble secondary phase, it should be selectively removed by acid treatment. To test this hypothesis, we evaluated samples before and after acid treatment by combining elemental distribution analysis by TEM-EDS, three-dimensional structural analysis by FIB-SEM, and chemical-state evaluation of aluminum by XPS. Whereas previous work20 reported the phenomenon of aluminum concentration within the HNL, the chemical form of aluminum, its location inside or outside the skeleton, and its influence on the functional properties were not clarified. The present study directly interrogates these points by combining selective leaching with complementary structural and chemical analyses.

Elucidating the HNL formation mechanism is directly relevant not only to the deliberate design of function but also to a general understanding of SAL formation in the aqueous corrosion of silicate glass. In particular, by suggesting that the two principal models—leaching / in-situ reorganization and ICDP—may contribute differently as a function of depth within a single alteration layer, this study provides new insight into a composite mechanistic model in the science of glass corrosion.[2,11]

Results

Cross sectional morphology and elemental redistribution

We first survey the cross-sectional structure of the HNL before and after acid leaching by STEM-HAADF observation. From Fig. 1a, a porous layer approximately 880 nm thick has formed near the glass surface in this specimen, corresponding to the HNL structure formed by alkaline etching. From Fig. 1b, the thickness of the HNL is confirmed to have decreased to approximately 790 nm in this specimen. This change may arise either from thinning due to leaching of HNL constituents or from partial detachment and loss of the porous layer, and the two cannot be distinguished from this observation alone. However, because a continuous porous layer is retained near the glass surface even after acid leaching, it is suggested that the HNL structure itself remains.

To identify the cause of this thickness change, we next evaluate the elemental distribution of the HNL cross-section by line profiles (Fig. 2). The line profiles shown in Fig. 2 are representative of the fields examined.
From Fig. 2a, the elemental distribution within the HNL agrees well with previous work: the HNL is composed mainly of Si, O, Al, and alkali-metal elements, and, compared with the bulk glass region, Al is concentrated while the Na concentration is reduced. In particular, the Al detection intensity increases gradually from near the surface, reaches a maximum (about two to three times the near-surface value) approximately 200 nm before the bulk interface, and then falls steeply as the interface is approached, converging to the level detected in the bulk interior. From Fig. 2b, the Na and Al signals within the HNL have almost disappeared.

Regarding the disappearance of Na, Na^+ can be released under acidic conditions by Na^+/H^+ exchange at non-bridging oxygen sites,[19] and the present observation is consistent with this mechanism. The porous HNL provides an extensive acid-accessible interface that can facilitate exchange throughout the layer. The near-complete loss of Al while a continuous porous silicate layer remained is less consistent with Al being predominantly incorporated as tetrahedral, network-forming AlO_4 species[23] and instead supports the presence of an acid-soluble Al-containing phase associated with the pore-wall region.

Surface chemical states

To verify the chemical form of aluminum more directly, XPS analysis of the Al 2p and O 1s spectra was performed; the results are shown in Fig. 3. Al 2p is sensitive to the oxidation and hydroxylation state of aluminum, whereas O 1s comprehensively reflects changes in the oxygen environment of the glass skeleton (bridging oxygen, non-bridging oxygen, hydroxyl groups, and so on); using the two spectra complementarily makes the interpretation of the surface chemical changes accompanying HNL formation more reliable.

From Fig. 3a, the Al 2p peak after HNL formation was shifted by 0.5 eV toward higher binding energy relative to untreated glass (74.9 versus 74.4 eV). Together with the acid-leaching behavior in Fig. 2b, this shift is consistent with a more hydroxylated, acid-soluble Al environment, but it does not by itself identify a unique crystalline phase.[22,24] After acid leaching, the Al signal was near or below the detection limit; the corresponding Al 2p spectrum was dominated by noise and was therefore excluded from peak-position analysis.

From Fig. 3b, the O 1s peak center remained within 532.6–532.7 eV for untreated, pre-leaching, and post-leaching samples, with no discernible shift among the measured conditions. The O 1s peak was broader before acid leaching than in untreated glass. As indicated by the peak fitting below, this broadening is consistent with contributions from additional oxygen environments, including the Al–OH and unassigned components.[24] After acid leaching, the peak narrowed and approached the line shape of untreated glass, consistent with loss of these additional components.

The main component at 532.7 eV was assigned to BO (Si–O–Si) and the low-energy component at 531.1 eV to NBO (Si–O–M). The assignments of BO (532.7 eV) and NBO (531.1 eV) in the O 1s spectrum are consistent with previous work on borosilicate glass reporting BO: 532.5 eV and NBO: 531.1 eV[25] (Fig. 3c). From Fig. 3c, no NBO component was found in the fitting analysis before acid leaching. This is considered to reflect the cleavage of Si–O–Na/K bonds by alkaline etching and the leaching of alkali-metal ions from the glass skeleton, consistent with previous findings.[21]

Before acid leaching, a new O 1s component was detected at 531.5 eV, a position distinct from that of NBO (Fig. 3c, blue line). The Al–OH-derived O 1s of $Al(OH)_3$ (crystalline gibbsite) is reported at 531.9 eV,[26] and 531.4 eV has been reported for $Al_2O_3/Al(OH)_3$;[22] the 531.5 eV of the present study agrees with these literature values within $\Delta E = 0.1–0.4$ eV and is not inconsistent with an assignment to Al–OH

bonds. In addition, a component was confirmed at 530.1 eV, at still lower binding energy (Fig. 3c, dashed line). This binding-energy region (529–530 eV) is generally assigned to metal oxides (M–O).[27] The glass used in this study is float glass, and it is known that tin derived from SnO and SnO_2 is incorporated into the tin side of float glass.[28] The O 1s of SnO_2 is reported at 530.2 eV,[29] close to the 530.1 eV obtained here. However, the fact that this component is not detected in the untreated sample and appears only after HNL formation is inconsistent with a simple detection of the tin layer on the float-glass surface. Surface oxidation accompanying alkaline corrosion, or local concentration of tin, may also be a contributing cause, but at present no clear basis for assignment has been obtained, and this component is treated as unassigned. Confirming the assignment would require additional investigation by complementary methods such as Sn 3d XPS or depth profiling.

After acid leaching, neither the Al–OH-derived component nor the unassigned component observed before acid treatment was resolved. This result is consistent with the near-complete depletion of Al in Fig. 2b and supports assignment of the Al–OH signal to an acid-soluble, hydroxylated Al-containing secondary phase. The origin of the unassigned component and the reason for its disappearance remain unresolved. Taken together, the Al 2p and O 1s spectra support a hydroxylated Al environment after HNL formation without establishing a unique crystalline aluminum hydroxide phase.

Depth dependent porous structure

Taken together, the TEM-EDS and XPS results support the interpretation that Al in the HNL is present predominantly as an acid-soluble, hydroxylated Al-containing secondary phase associated with the silicate skeleton rather than incorporated uniformly as a network-forming species. We therefore examined how removal of this Al-containing material affected the depth distributions of porosity and segmented-solid diameter obtained by FIB-SEM tomography.
Figure 4 shows representative HNL/bulk-interface-referenced profiles of porosity and mean segmented-solid diameter before and after acid leaching. The HNL/bulk-glass interface is defined as 0 nm, and the positive direction points toward the outer surface. The profiles are representative measurements of the displayed specimens rather than statistical averages; absolute values, including layer thickness, vary among specimens.

Porosity (Fig. 4a): in the sample after acid leaching, the porosity increases almost linearly from the bulk interface to the outermost surface (interface: porosity ≈ 0%; outermost surface: porosity ≈ 50%). In the sample before acid leaching, by contrast, the rise in porosity from the interface toward the surface is gentler, increasing with undulations over a range of about 100 nm from the interface and reaching a porosity ≈ 40% near the outermost surface. As a result, there is almost no difference in porosity between the two in the range about 100–300 nm from the interface, whereas closer to the surface the porosity after acid treatment clearly exceeds that before acid treatment. Moreover, when the gradient itself rising from the bulk interface (porosity 0%) is compared, that of the sample after acid treatment is steeper than that before acid treatment. This point is related to the interpretation of the reflectance spectrum described later (Fig. 5).

Mean segmented-solid diameter (Fig. 4b): after acid leaching, the measured diameter was approximately 10 nm smaller across the analyzed HNL depth (from about 30 to 20 nm near the surface and from about 40 to 30 nm near the interface). This decrease is consistent with recession of the segmented solid phase following removal of acid-soluble Al-containing material, although a minor contribution from silicate dissolution cannot be excluded.

The changes in porosity and skeleton diameter appear, at first sight, to be contradictory. If the skeleton diameter decreases uniformly across the whole HNL, the removed volume should be added to the pore side and the porosity should therefore also increase markedly across the whole HNL; in practice, however, almost no change in porosity is seen near the interface.

Interpretation of the asymmetric behavior of porosity and skeleton diameter, and of the depth dependence of the Al detection intensity

The depth dependence of the Al signal in Fig. 2a, which reaches a maximum about 200 nm from the interface and then decreases toward the bulk, should be interpreted together with the porosity and segmented-solid-diameter profiles in Fig. 4. Because the characteristic pore size decreases toward the bulk interface, the skeletal surface area per unit volume is expected to increase in that direction, although specific surface area was not measured directly. Consequently, if the hydroxylated Al-containing secondary phase is associated with pore walls, the depth-dependent EDS intensity could reflect both its local abundance and the available interfacial area.

Separating this interfacial-area effect from a true change in the local abundance of the Al-containing phase would require reliable pore-size measurements near the interface. In that region, however, the pore dimensions approach the effective resolution of the present FIB-SEM dataset. The current data therefore do not resolve the relative contributions of interfacial area and local composition to the Al-intensity profile.

Two levels of inference should therefore be distinguished. First, the near-complete loss of the Al and Al–OH signals after acid treatment supports the presence of an acid-soluble secondary phase associated with the silicate skeleton. Second, the detailed spatial arrangement of this phase—such as a thin pore-wall-associated layer, localized deposits, or partial filling of fine pores—is not resolved by the present data and requires higher-resolution structural or complementary surface-area measurements.

The apparently different responses of segmented-solid diameter and porosity may likewise be influenced by the depth-dependent geometry. Near the surface, removal of pore-wall-associated material can be expressed directly as an increase in pore volume. Near the interface, where features are finer and segmentation is more sensitive to local connectivity, a small amount of removed material may alter the local-thickness metric without producing an equally apparent change in area-fraction porosity. This explanation is a plausible interpretation rather than a uniquely determined structural model.

In this way, changing the acid-leaching conditions (pH, treatment time, presence or absence of ultrasonication, and so on) alters the skeleton-diameter and porosity distributions of the HNL, and is considered to affect both the optical response (reflectance) and the wettability. In the following, we evaluate the reflectance spectra and the spreading behavior of water droplets before and after acid leaching, and examine the correspondence between the structural changes and the functional changes.

Optical response

Figure 5 shows the reflectance spectra of the HNL glass before and after acid leaching. In the sample after acid leaching, the interference peaks shifted toward shorter wavelengths. This shift corresponds to a decrease in the effective optical thickness and reflects the thickness reduction of the HNL.

After acid leaching, the measured reflectance was approximately 0.1–0.2% higher across the measured wavelength range. A plausible interpretation is that the steeper porosity gradient near the HNL/bulk-glass interface after leaching produces a sharper effective-refractive-index transition and hence a larger interfacial-reflection contribution. Because the reflectance depends on the complete depth-dependent optical profile and the observed difference is small, this assignment should be regarded as consistent with, rather than uniquely demonstrated by, the structural data in Fig. 4a.

The optical properties exhibited by the HNL have been shown by previous work to be closely related to the surface wettability, and it is expected that if the skeleton and pore structure change upon acid leaching, a corresponding change will appear in the spreading behavior. We therefore next evaluated, for the same samples, the change in wettability and infiltration properties using the spreading behavior of a water droplet as an indicator.

Wetting response

Figure 6 shows the time evolution of the projected area of a water droplet before and after acid leaching. The smaller initial projected area after leaching is consistent with a reduction in the effective capillary driving force, although projected-area measurements alone do not uniquely separate spreading from infiltration. Skeleton thinning may increase the effective pore size and thereby reduce the capillary pressure, $\Delta P \propto \cos\theta/d$, while changes in the effective contact angle may also contribute.

The removal of Al–OH-containing material also changes the pore-wall surface chemistry and may therefore alter the surface free energy and effective contact angle. Nevertheless, the observed increase in near-surface porosity and decrease in segmented-solid diameter favor enlargement of the effective pores as the main contributor to the reduced spreading, with a concurrent contribution from surface-chemical changes.

Before acid leaching, the projected droplet area increased monotonically after deposition, consistent with progressive spreading and/or liquid uptake by the porous layer. After acid leaching, the projected area changed less and approached a nearly constant value more rapidly, consistent with a reduced capillary driving force. The subsequent decrease in projected area was faster before leaching, which may

reflect the larger initial wetted area or liquid content. Similar late-stage slopes suggest comparable apparent area-loss kinetics, but projected-area measurements alone do not identify a unique evaporation or infiltration rate-limiting mechanism.

Taken together, acid leaching depleted the hydroxylated Al-containing secondary phase, altered the nanoscale segmented-solid and porosity profiles, and was accompanied by changes in reflectance and water-droplet spreading. These functional responses are consistent with the structural changes identified by FIB-SEM, STEM-EDS, and XPS and show that selective post-corrosion treatment can modulate the optical and wetting response of the HNL.

Discussion

Combined FIB-SEM, STEM-EDS, and XPS observations support the presence of an acid-soluble, hydroxylated Al-containing secondary phase associated with the HNL skeleton. The persistence of a continuous porous silicate layer after near-complete Al depletion argues against Al being predominantly incorporated as a network-forming species throughout the skeleton. This finding supports the involvement of an ICDP-type process in which dissolved aluminum species re-precipitate near the alteration-layer skeleton. Because the experiment compares states before and after treatment rather than observing precipitation in situ, it supports but does not independently prove the proposed pathway.

Removal of the Al-containing phase was accompanied by an approximately depth-independent decrease in measured segmented-solid diameter, whereas the porosity increase was concentrated toward the outer region. The different responses of these metrics may arise from depth-dependent interfacial area, connectivity, and segmentation sensitivity. The present resolution does not distinguish a conformal pore-wall-associated phase from localized deposits or partial filling of fine pores, but the observations constrain viable structural models for aluminum retention in the HNL.

The spectral blue shift is consistent with reduced optical thickness, while the small reflectance increase is plausibly associated with the sharper porosity gradient near the HNL/bulk-glass interface. The wetting data likewise indicate reduced droplet spreading after leaching. Changes in skeleton-surface free energy probably contribute, but the structural observations favor effective pore enlargement after skeleton thinning as the main contributor. These interpretations remain appropriately limited because the reflectance difference is small and projected droplet area combines spreading, infiltration, and evaporation.

Overall, the results support a composite picture in which leaching/in situ reorganization and ICDP-type processes both contribute to HNL formation. Sodium depletion is consistent with ion-exchange leaching, whereas the acid-removable hydroxylated Al-containing phase is consistent with dissolution followed by local retention or re-precipitation. Aluminum speciation therefore emerges as an important variable linking corrosion chemistry to alteration-layer structure and functional response. Selective post-corrosion leaching further provides an experimental route for testing these structure–property relationships.

Materials and Methods

Substrates and pretreatment

Commercial borosilicate glass (TEMPAX Float®, Schott Jenaer Glas GmbH) was used as the substrate. As a pretreatment, the substrates were ultrasonically cleaned in acetone, methanol, and deionized water for 10 min each.

HNL fabrication

The HNL was formed by heat etching the substrate in a 0.1 mol L^{-1} disodium hydrogen phosphate (Na_2HPO_4; reagent special grade, FUJIFILM Wako Pure Chemical) aqueous solution at 120°C for 30 h. Na_2HPO_4 was selected as the corrosion medium because previous work reported no essential difference in HNL formation behavior between $NaHCO_3$ and phosphate-based solutions,[20] while the Na_2HPO_4 solution is chemically stable even under prolonged heating and therefore provides highly reproducible corrosion conditions.

Acid leaching

Hydrochloric acid (HCl; reagent special grade, FUJIFILM Wako Pure Chemical) adjusted to pH 1.6 was used. This pH was selected because $Al(OH)_3$ becomes soluble below pH ≈ 4,[24] whereas silica dissolution is comparatively slow under these acidic conditions. The treatment was therefore designed to favor removal of the acid-soluble Al-containing phase while limiting, but not assuming the complete absence of, silicate dissolution. The HNL glass was immersed in the acid solution and ultrasonicated in a separate-type W-115 unit (Echotec; rated output 300 W, 100% output) for 10 min. The samples were then thoroughly rinsed with deionized water and dried before analysis.

FIB-SEM three-dimensional reconstruction

An orthogonal FIB-SEM instrument (SMF-1000, Hitachi High-Tech, Tokyo) was used. After the sample interior was impregnated with epoxy resin (G-2, part no. 780028520, JEOL Ltd), sequential FIB cross-sectional milling and SEM imaging were repeated to acquire a stack of serial cross-sectional images.

Alignment (drift correction)

In FIB-SEM observation, the field of view drifts between slices owing to charging by electron-beam irradiation and stage instability. Drift was corrected by computing the cross-correlation function between two consecutive images, finding the shift that maximized the correlation, and translating the image accordingly; this operation was applied throughout the stack.

Binarization (separation of skeleton and pores)

Because the HNL exhibits a depth-dependent pore structure, charging and image brightness also vary with depth, making use of one global threshold inappropriate. After three-dimensional reconstruction, the data were therefore re-sliced into planes perpendicular to the depth direction. A slice-specific threshold

was selected from the brightness histogram, with bimodality used where discernible, after correction of the depth-dependent brightness variation. Pixels above and below the threshold were classified as segmented solid and pore, respectively. Fiji/ImageJ with the BoneJ plugin was used for the analysis.

Porosity distribution analysis

For each binarized cross-sectional image, the tomographic data were re-sliced parallel to the HNL/bulk-glass interface, and porosity was calculated from the fraction of pixels classified as pores at each depth. This area-fraction metric avoids the geometric assumptions of the maximum-inscribed-sphere analysis, but it remains dependent on image contrast, resolution, and threshold selection.

Dimensional evaluation: maximum-inscribed-sphere method (local-thickness analysis)

The segmented-solid-diameter distribution was evaluated by the maximum-inscribed-sphere method applied to the binarized three-dimensional volume. For each voxel in the segmented-solid region, the diameter of the largest sphere containing that voxel without crossing the region boundary was assigned as the local diameter; spheres wholly contained within larger spheres were excluded. The mean local diameter was then calculated as a function of depth. The same procedure was explored for pores, but near the bulk interface their dimensions approached the spatial sampling of the FIB-SEM dataset (3 nm pixel^{-1}). Reliable discrimination generally required a feature to span approximately 3–5 pixels under the available contrast and noise, corresponding to an effective lower range of about 9–15 nm. Pore-diameter profiles were therefore not interpreted quantitatively, and porosity and segmented-solid diameter were used as the principal structural descriptors.

Cross-sectional analysis by STEM

TEM sample preparation. The sample surface was protected with the same epoxy resin used for FIB-SEM observation. The resin-coated sample was sectioned with a low-speed cutter (Isomet, model 11-1280-170, BUEHLER, Lake Bluff, IL, USA). The resulting cross-section was polished to a thickness of 110 μm using diamond lapping film (abrasive particle diameter 9 μm). After polishing, the sample was thinned with an ion slicer (EM-09100IS, JEOL Ltd) until the final thickness was below 100 nm and was then given a final finishing polish with a precision ion polishing system (PIPS) to reduce artifacts introduced during sample preparation. The PIPS treatment used initial conditions of an accelerating voltage of 2.0 kV, an incidence angle of ± 8°, a rotation speed of 2.0 rpm, and a processing time of about 15 min; the accelerating voltage (1.5 kV → 1.0 kV) and rotation speed (1.5 rpm → 1.0 rpm) were reduced stepwise as thinning progressed.

STEM-HAADF observation and EDS elemental analysis. A scanning transmission electron microscope (STEM; JEM-ARM200F, JEOL Ltd, Tokyo) was used, equipped with a silicon-drift EDS detector (Dry SD100GV, JEOL Ltd, Tokyo). The EDS conditions were an accelerating voltage of 200 kV, a probe setting

of 5C, and a condenser aperture of 40 μm. Elemental maps were acquired with an acquisition time of at least 10 min and a resolution of 256 × 256 pixels.

Data processing. Spectra were processed with NSS (Noran System Seven) analysis software (Thermo Fisher Scientific, Waltham, MA, USA). The net counts of each element were determined after background subtraction. The line profiles shown in this paper were generated by integrating the elemental-map data along the in-plane direction.

Chemical-state analysis by XPS

An X-ray photoelectron spectrometer (SSX-100, Surface Science Instruments, Mountain View, CA, USA) was used with a monochromated Al Kα source. To suppress the influence of charging in the insulating samples, a flood gun was used. For the binding-energy reference, previous work has shown that the skeleton composition of the HNL is close to that of silica glass (SiO_2),21 and Si 2p = 103.3 eV (the SiO_2 reference value)22 was used as an internal standard to ensure the objectivity and reproducibility of the charge correction. Although referencing to the C 1s of surface-adsorbed hydrocarbons (284.8 eV) is also a common method for insulating glass samples, the amount and state of adsorbed carbon can vary depending on the surface chemistry of the sample (for example, the presence of Al(OH)□), and surface chemical heterogeneity has been reported to affect the hydration and adsorption behavior of silica surfaces;30 referencing instead to the Si 2p of the intrinsic SiO_2 skeleton therefore ensures higher consistency between samples before and after acid treatment and with the untreated sample. Al 2p and O 1s spectra were acquired. For Al 2p, the change in the chemical form of aluminum was evaluated by comparing the peak-position shift between the untreated glass and the sample before acid leaching. For O 1s, spectra were acquired for three conditions—untreated glass and the samples before and after acid leaching—and, after Shirley background subtraction, multi-component peak fitting with Voigt functions was performed to compare the oxygen environments among the three conditions. The fitting was used qualitatively to assess the presence or absence of resolved components; fitted component areas were not used for absolute compositional quantification. Na was excluded from this analysis because the binding energy of Na 1s is high (about 1071 eV), the corresponding photoelectron kinetic energy is small so that the escape depth is shallow, the detection sensitivity is low, and it is unsuitable for chemical-state discrimination.

Reflectance measurement (optical response to structural change)

Reflectance spectra before and after acid treatment were acquired with an MSP-100 instrument (Shibuya Optical) over 400–900 nm. The spectra were used to compare changes in interference features and overall reflectance associated with the HNL thickness and depth-dependent effective refractive index. The displayed spectra are representative measurements of the specimens shown; no inferential statistical comparison was performed.

Time-resolved droplet-area measurement (wetting response to structural change)

The wetting response was evaluated from the time evolution of projected water-droplet area before and after acid treatment. A 2 μL droplet of deionized water was deposited with a microsyringe, and its projected shape was recorded every 20 s from immediately after deposition. The projected area was obtained by image analysis. This observable reflects the combined effects of lateral spreading, liquid uptake into the porous layer, and evaporation and was therefore not interpreted as a direct measurement of any one process in isolation.

Statistics and reproducibility

HNL fabrication and acid-leaching behavior were repeatedly examined across at least ten independently prepared specimens during the experimental program. For microscopy, multiple candidate fields of view —typically approximately five—were inspected, and the images and profiles presented here were selected as representative observations. Exact specimen and field counts were not prospectively fixed for each characterization method; no inferential statistical tests were therefore applied, and no P values are reported. Quantitative profiles in Figs. 4–6 should be interpreted as representative measurements of the displayed specimens rather than population estimates.

Declarations

Author contributions

T.H. and T.F. conceptualized the study. T.H., S.M., I.F. and R.K. performed the experiments and analyzed the data. T.H. and T.F. wrote the manuscript. T.F. supervised the study. All authors reviewed and approved the final manuscript.

Acknowledgements

This work was supported by JSPS KAKENHI Grant Numbers 22H02171 and 23K23439. TEM-EDS experiments were supported by the Advanced Research Infrastructure for Materials and Nanotechnology (ARIM) at The University of Tokyo. FIB-SEM experiments were supported by the ARIM program at the National Institute for Materials Science (NIMS). This work was partly supported by the TOKYO CITY UNIVERSITY Interdisciplinary Research Center for Nano Science and Technology for instrumental analysis. The authors appreciate the support of M. Morikawa (Tokai University) with the XPS measurements. The funders had no role in study design, data collection, analysis and interpretation of data, or preparation of the manuscript.

Competing interests

All authors declare no financial or non-financial competing interests.

Data Availability

The raw and processed datasets generated in this study, including FIB-SEM image stacks, STEM-EDS maps and line profiles, XPS spectra, reflectance spectra, and time-resolved droplet-area data, are available from the corresponding author upon reasonable request.

Code availability

No custom code was developed for this study. Image processing was performed using Fiji/ImageJ and the BoneJ plugin as described in the Methods.

References

1. Gin, S. et al. An international initiative on long-term behavior of high-level nuclear waste glass. *Mater. Today* **16**, 243–248 (2013).
2. Gin, S., Delaye, J.-M., Angeli, F. & Schuller, S. Aqueous alteration of silicate glasses: state of knowledge and perspectives. *npj Mater. Degrad.* **5**, 42 (2021).
3. Lin, Y.-T. et al. Glass–water interactions: from surface into the bulk. *J. Am. Ceram. Soc.* **108**, e70137 (2025).
4. Jégou, C., Gin, S. & Larché, F. Alteration kinetics of a simplified nuclear glass in an aqueous medium: effects of solution chemistry and of protective gel properties on diminishing the alteration rate. *J. Nucl. Mater.* **280**, 216–229 (2000).
5. Gin, S. et al. Origin and consequences of silicate glass passivation by surface layers. *Nat. Commun.* **6**, 6360 (2015).
6. Gin, S. et al. Dynamics of self-reorganization explains passivation of silicate glasses. *Nat. Commun.* **9**, 2169 (2018).
7. Geisler, T. et al. Aqueous corrosion of borosilicate glass under acidic conditions: a new corrosion mechanism. *J. Non-Cryst. Solids* **356**, 1458–1465 (2010).
8. Hellmann, R. et al. Nanometre-scale evidence for interfacial dissolution–reprecipitation control of silicate glass corrosion. *Nat. Mater.* **14**, 307–311 (2015).
9. Geisler, T. et al. The mechanism of borosilicate glass corrosion revisited. *Geochim. Cosmochim. Acta* **158**, 112–129 (2015).
10. Geisler, T. et al. Real-time in situ observations of reaction and transport phenomena during silicate glass corrosion by fluid-cell Raman spectroscopy. *Nat. Mater.* **18**, 342–348 (2019).
11. Gin, S. et al. A general mechanism for gel layer formation on borosilicate glass under aqueous corrosion. *J. Phys. Chem. C* **124**, 5132–5144 (2020).
12. Fujima, T., Futakuchi, E., Tomita, T., Orai, Y. & Sunaoshi, T. Hierarchical nanoporous glass with antireflectivity and superhydrophilicity by one-pot etching. *Langmuir* **30**, 14494–14497 (2014).
13. Tabata, E. et al. Fingerprint blurring on a hierarchical nanoporous layer glass. *Coatings* **9**, 653 (2019).

14. Minegishi, S. et al. Highly water repellent and anti-reflective glass based on a hierarchical nanoporous layer. *Coatings* **12**, 961 (2022).
15. Shinozaki, K. et al. Fabrication of a robust organic–inorganic perovskite nanoparticle dispersion layer on a glass surface. *Ceram. Int.* **50**, 14113–14117 (2024).
16. Fujima, T., Kawai, K., Okabe, T. & Ito, T. A PSS-free PEDOT conductive film supported by a hierarchical nanoporous layer glass. *Macromol. Mater. Eng.* **303**, 1800183 (2018).
17. Bunker, B. C. Molecular mechanisms for corrosion of silica and silicate glasses. *J. Non-Cryst. Solids* **179**, 300–308 (1994).
18. Smets, B. M. J. & Lommen, T. P. A. The leaching of sodium containing glasses: ion exchange or diffusion of molecular water? *J. Phys. Colloques* **43** (C9), C9-649–C9-652 (1982).
19. Deng, L. et al. Ion exchange mechanisms and interfacial reaction kinetics during aqueous corrosion of sodium silicate glasses. *npj Mater. Degrad.* **5**, 15 (2021).
20. Maeda, S., Funayama, I., Motegi, N. & Fujima, T. Elemental distribution analysis of mesoporous structure on silicate glass surface corroded in K_2HPO_4 aqueous solution. *J. Non-Cryst. Solids* **690**, 124256 (2026).
21. Ito, T., Tabata, E., Ushioda, Y. & Fujima, T. Effect of boron in a hierarchical nanoporous layer formation on silicate glass. *Materials* **13**, 1817 (2020).
22. Wagner, C. D. et al. *NIST Standard Reference Database 20: NIST X-ray Photoelectron Spectroscopy (XPS) Database, Version 3.4* (National Institute of Standards and Technology, Gaithersburg, MD, 2003).
23. Damodaran, K., Delaye, J.-M., Kalinichev, A. G. & Gin, S. Deciphering the non-linear impact of Al on chemical durability of silicate glass. *Acta Mater.* **225**, 117478 (2022).
24. Gayer, K. H., Thompson, L. C. & Zajicek, O. T. The solubility of aluminum hydroxide in acidic and basic media at 25 °C. *Can. J. Chem.* **36**, 1268–1271 (1958).
25. Pintori, G. & Cattaruzza, E. XPS/ESCA on glass surfaces: a useful tool for ancient and modern materials. *Opt. Mater. X* **13**, 100108 (2022).
26. Kloprogge, J. T., Duong, L. V., Wood, B. J. & Frost, R. L. XPS study of the major minerals in bauxite: gibbsite, bayerite and (pseudo-)boehmite. *J. Colloid Interface Sci.* **296**, 572–576 (2006).
27. Dupin, J.-C., Gonbeau, D., Vinatier, P. & Levasseur, A. Systematic XPS studies of metal oxides, hydroxides and peroxides. *Phys. Chem. Chem. Phys.* **2**, 1319–1324 (2000).
28. Baitinger, W. E., French, P. W. & Swarts, E. L. Characterization of tin in the bottom surface of float glass by ellipsometry and XPS. *J. Non-Cryst. Solids* **38–39**, 749–754 (1980).
29. Ibrahim, Z., Othaman, Z., Karim, M. M. A. & Holland, D. X-ray photoemission spectroscopy (XPS) analysis on platinum doped stannic oxide ceramic. *Solid State Sci. Technol.* **15**, 65–73 (2007).
30. Schrader, A. M. et al. Surface chemical heterogeneity modulates silica surface hydration. *Proc. Natl. Acad. Sci. U.S.A.* **115**, 2890–2895 (2018).

Figures

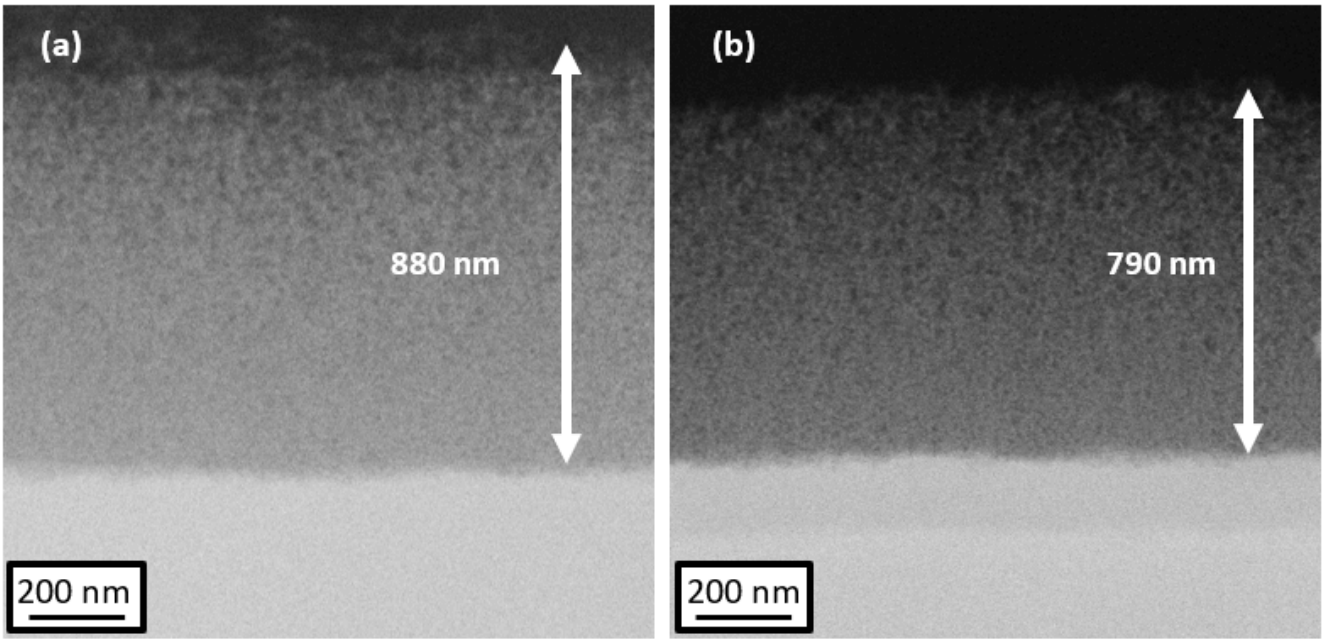


Figure 1

Cross-sectional STEM-HAADF images of the HNL glass before and after acid leaching: (a) pre-leaching, (b) post-leaching. The double-headed arrows indicate the thickness of the HNL structure.

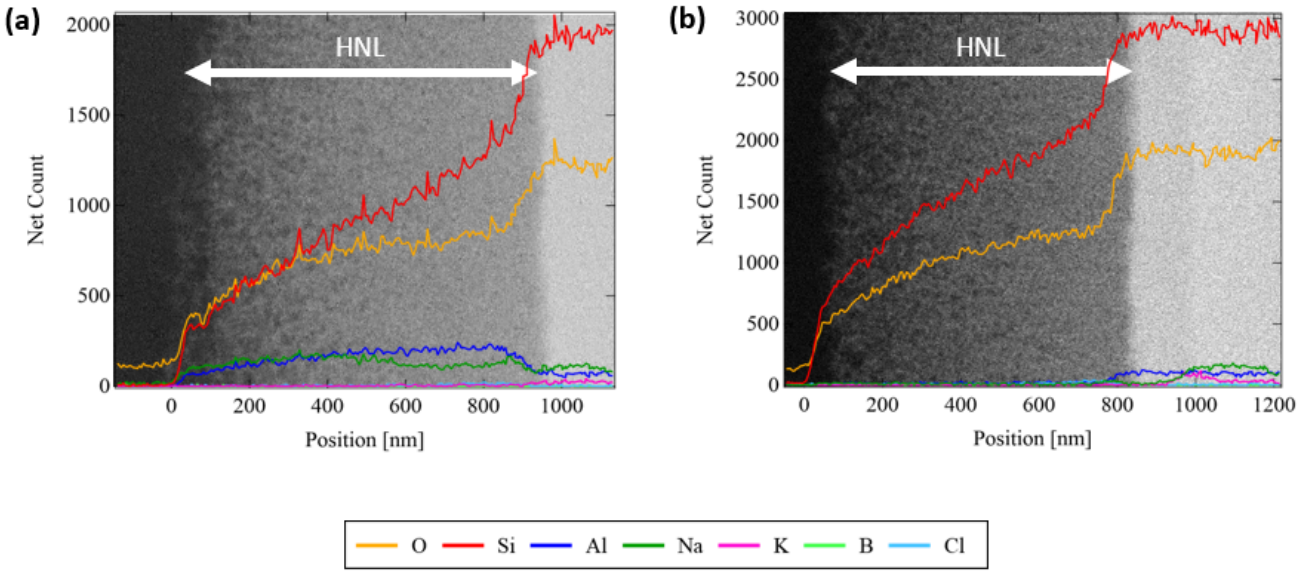


Figure 2

Elemental distribution (line profiles) of HNL glass before and after acid leaching: (a) pre-leaching, (b) post-leaching, superimposed on the corresponding STEM-HAADF images.

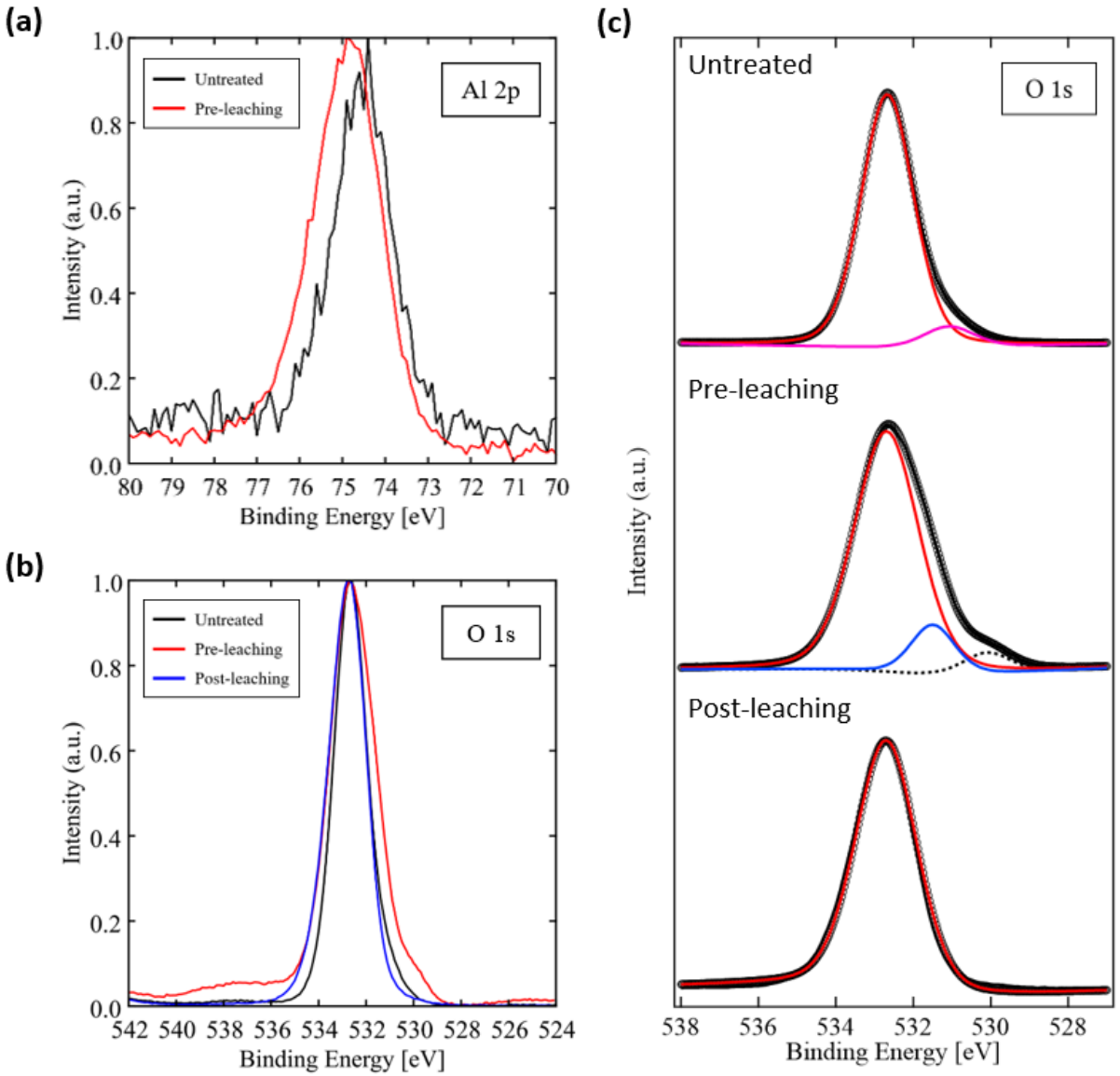


Figure 3

XPS spectra of HNL glasses before and after acid leaching and untreated glass: (a) Al 2p spectra (untreated and pre-leaching), (b) O 1s spectra (untreated, pre-leaching, and post-leaching), (c) O 1s spectra and peak-fitting results for the untreated, pre-leaching, and post-leaching conditions. The solid black line is the measured spectrum, the open black circles are the fitted envelope, the red line is bridging oxygen (BO), the pink line is non-bridging oxygen (NBO), the blue line is the Al–OH component, and the dashed line is the unassigned component.

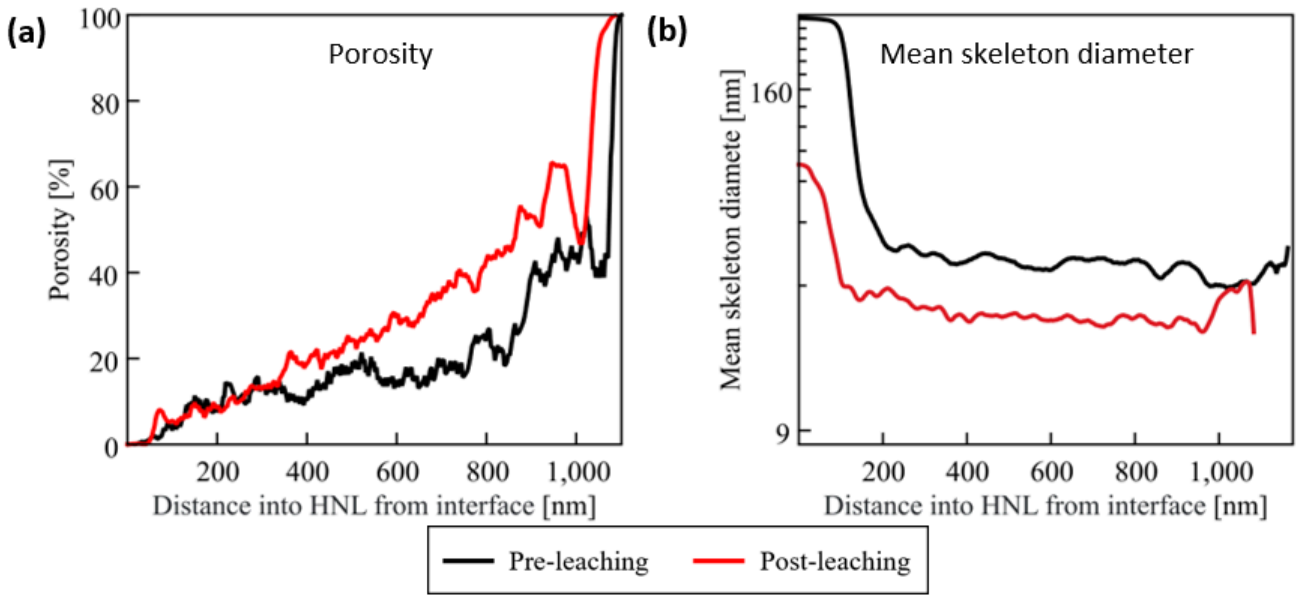


Figure 4

Depth distributions of porosity and mean skeleton diameter within the HNL glass before and after acid leaching. The horizontal axis indicates the distance from the HNL/bulk interface toward the surface: (a) Porosity, (b) mean skeleton diameter.

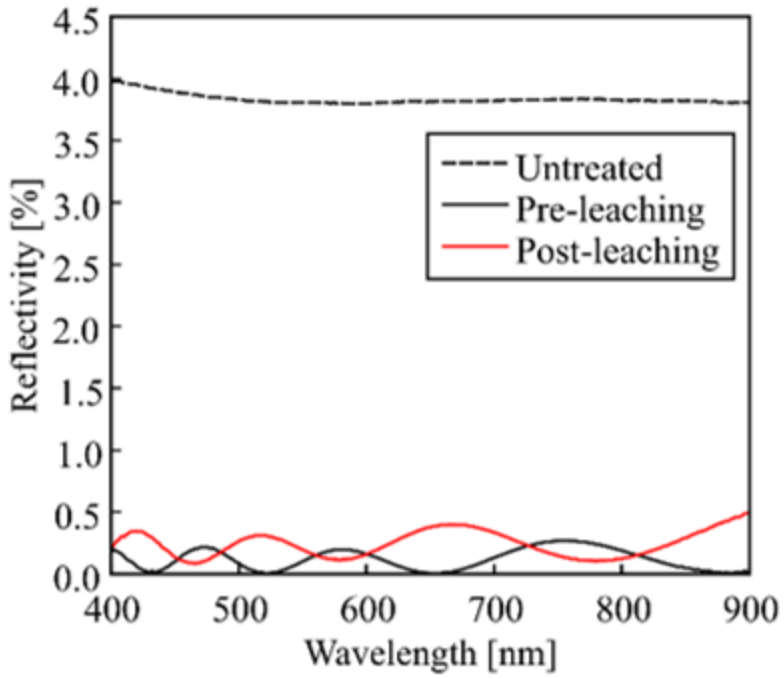


Figure 5

Reflectance spectra of the HNL glass before and after acid leaching.

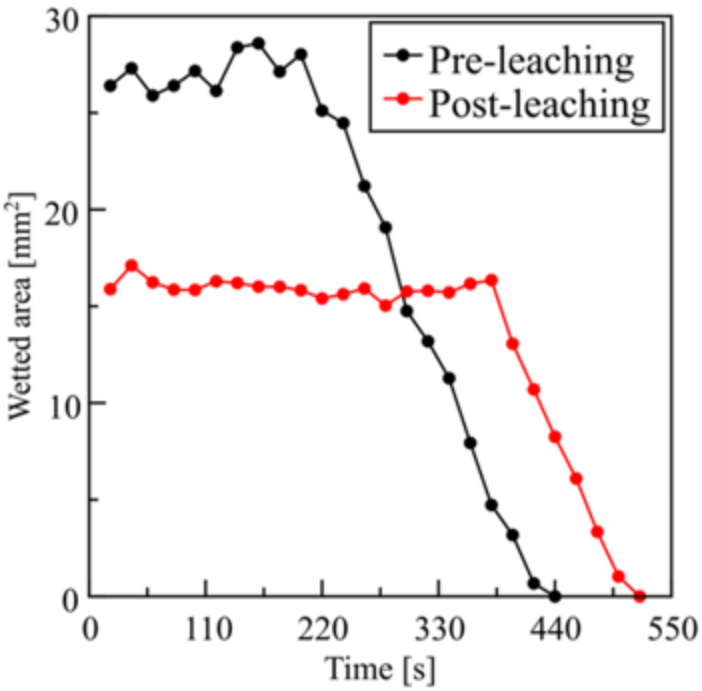


Figure 6

Time evolution of the projected area of a water droplet before and after acid leaching.